Proc. of SPIE Vol. 0332, Advanced Technology Optical Telescopes I, ed. L.D. Barr, G. Burbidge (Jan 1982) Copyright SPIE

Gravity deflections of lightweighted mirrors

D. Anderson, R. E. Parks
Optical Sciences Center, University of Arizona, Tucson, Arizona 85721
Q. M. Hansen, R. Melugin
NASA/Ames Research Center, Moffett Field, California 94035

Abstract

Two 20-in. diameter, f/4 fused silica mirrors were lightweighted by contouring the rear sides to near parabolic cross sections. One mirror was lightweighted into a single-arch, thick-hub design. The other mirror took the form of a cantilevered double arch. Details of the fabrication are outlined. Following fabrication, these mirrors were interferometrically tested at their centers of curvature in both a face-up and face-down support mode. By subtracting the wavefront errors in these two support modes, the gravity deflections were determined in spite of some residual figure error. Details of the data analysis and the resulting gravity-induced deflections are reported. These empirical results are compared with finite element analyses with favorable results.

Introduction

Fused silica has long been known to be an excellent optical material to fabricate, but more importantly it is available with high uniformity of expansivity at cryogenic temperatures.[1,2] With the promise of small thermally induced surface errors from highly uniform fused silica, NASA Ames Research Center sponsored the design and analysis of two 20-in. lightweight mirrors,[3] their fabrication and test, which are reported in this paper, and the tests of one of the mirrors at 10^{o}K.[4] The quartz materials used for the mirrors were Corning Code 7940 fused silica made by a flame hydrolysis process and Heraeus TO-8 Commercial Type E Composite Material made by the fusion of natural quartz. The mirrors were lightweighted by tapering the backside in two different configurations: a single-arch design and a double-arch design (see Figure 1). This method of lightweighting can reduce the mass to roughly 1/2 to 1/3 that of the equivalent right circular cylinder.

These mirrors provide an opportunity not only to test the two types of material at extremely low temperatures but also to investigate the relative merits of the two lightweight shapes with respect to the ease of fabrication and the degree of figure deflection due to self-weight.

This method of lightweighting the mirrors was chosen over the more conventional egg-crate and membrane-and-ribs methods for two closely related reasons: (1) the relative ease of fabrication and (2) the resultant decrease in cost. The optical surfaces were to be f/4 spheres (80-in. radius of curvature) for ease of fabrication and monitoring the figure during cryogenic testing.

Fabrication

The fused silica blanks were Blanchard ground to accurate right-circular cylinders 20 in. in diameter by 4 in. thick before they were delivered to the Optical Sciences Center. The first mirror processed was the Heraeus natural fused quartz. This mirror blank was made into the single-arch version. The central hole core was drilled with a 5-in. diameter core drill mounted in a Bridgeport mill. The process took about 1/2 hour to accomplish. The blank was then placed face up on a 60-in. Strasbaugh polishing machine equipped with a cam-controlled generator. The thickness of the single arch blank was reduced to 3.5 in. and then the 80-in. radius was generated using the cam-following generator. The same steps

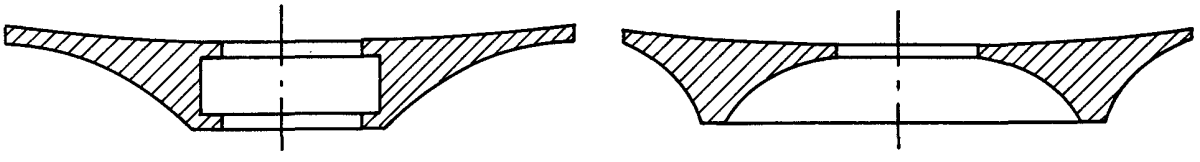

Figure 1. Cross sections of the single and double arch mirrors.

were then performed on the Corning blank, which was made into a double arch, but the thickness was maintained at 4 in. Generation of the front was done on both blanks before work was performed on the back because the flat back gave good support during generation of the spherical surfaces.

The blanks were then turned over and held down on the polishing machine with optician's wax and thin edge blocks. Cam templates had previously been cut to the contours shown in Figure 1 for controlling the rear contours. The appropriate cam was mounted on the generator and a peripheral wheel was used for lightweighting. The generator was pulled up the templates by the lead screw of the generator. The slope on the single arch was shallow enough that this operation proceeded smoothly and took about 25 hours of generating time to finish. Figure 2 shows the equipment for generating the mirror surfaces.

The slope on the double arch was sufficiently steep that this contour was difficult to accomplish. The generator was never intended for cutting slopes this steep although the machine can be modified in the future to handle this situation better. Generating the double arch took about 100 hours including time to reset the machine to do the inside arch.

After lightweighting, the mounting recesses and holes were added to the mirrors using core drills on the Bridgeport mill. The contoured backs were lapped with flexible tile pads and 80 silicon carbide abrasive to remove the generator marks and to give the surface a uniform matte finish.

Following this lapping, both mirrors were etched to relieve any residual stresses due to the processing to this point. The mirrors were submerged in a room-temperature, 15% solution by volume of ammonium bifluoride. The solution was gently agitated for one hour after which time the mirror was removed and rinsed thoroughly with tap water followed by a rinse of distilled water. Ammonium bifluoride was used instead of hydrofluoric acid because it is innocuous compared to the acid yet just as effective at removing glass though at a somewhat slower pace.

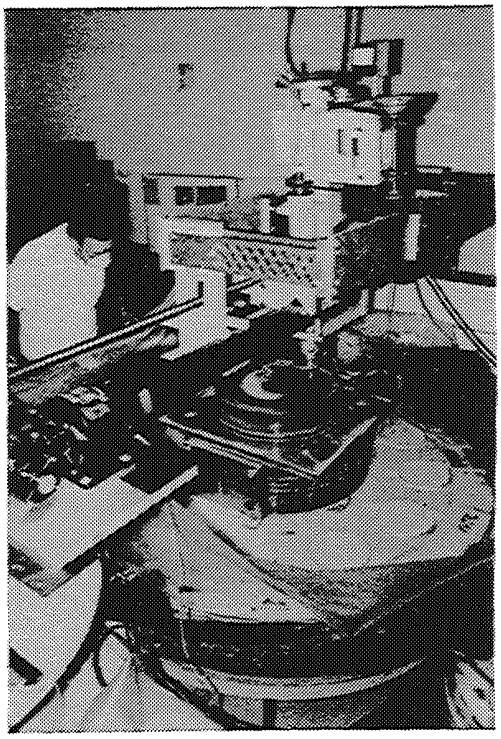

Figure 2. Optician Bob Crawford at the helm of the generator generating the front surface of the single arch.

At this point the fabrication process for the two mirrors differed somewhat. The single arch mirror was lapped and polished spherical to the 80-in. radius. It was then heat treated in an electric oven to 575°C to bake on a silver paint that was applied to the rear of the mirrors for use in attaching heat conductors for cryogenic cooling. The double arch was heat treated immediately after etching and was then lapped and polished spherical.

The single arch mirror was interferometrically tested both before and after heating to see if any figure change had occurred. The figure appears to have changed about 0.5 λ peak-to-valley in a somewhat three-corned way. We believe this change in figure is real and was probably due to the way in which the mirror was supported and heated. It was heated face down on three firebricks spaced about 120 degrees apart and heated with a single thermocouple control located on the thick hub. The thin edge of the mirror not in contact with the firebricks may have become considerably hotter than the thick hub when the hub reached its maximum 575°C temperature. Upon cooling, this may have induced some slight strain in the glass causing the figure change.

The double arch mirror was heated much more slowly than the single arch: 3.5 hours to reach maximum temperature versus 20 minutes for the single arch, and with its face up. No optical testing was done on the double arch at this stage because the mirror had not yet been polished.

The two mirrors were very similar in degree of difficulty during manufacture with the exception of the steeper curves on the double arch, which increased the difficulty of that mirror. Otherwise, the fabrication of the two mirrors was virtually identical and not difficult.

Optical testing: determination of the gravity deflections

The question to be answered by optical testing of the two mirror shapes was which shape would be least subject to gravity-induced deflections when the mirrors were moved from a 1-g load environment to a 0-g or weightless environment. Since it is difficult to create a 0-g environment in which to test the mirrors, it was decided to shift the load on the mirrors from +1 g to -1 g, then take the difference in the deflections in these two orientations and divide by two to deduce the expected deformation during a load change from 1 g to 0 g.

Both mirrors were tested on their backs while supported by three ball bearings spaced 120 degrees apart under their hubs. This test was defined as the 1-g case. The mirrors were then turned upside down and supported at the same locations with the three ball bearings on the ends of a simple spider mount. These test setups are shown in Figure 3. The face-down position was defined as the -1-g case. In both cases a folding flat was used to shift the center of curvature of the mirror to a more convenient position for the interferometer and camera.

Two fiducials placed approximately 90 degrees apart were attached to the periphery of the mirror and three small fiducials were positioned around the center hole pointing to the locations on the hub of the three-ball supports. A Shack interferometer operating at 6328 Å was used to produce interference fringes that were photographed on 4-in. x 5-in. Polaroid high-speed film.

Four interferograms were taken at each test position and the results of the interferogram reductions were averaged to help minimize the error contribution from air turbulence, vibration, and other random noise. The FRINGE data reduction program was used to reduce the interferograms so that the mirror's surface was described by a set of 36 Zernike polynomial

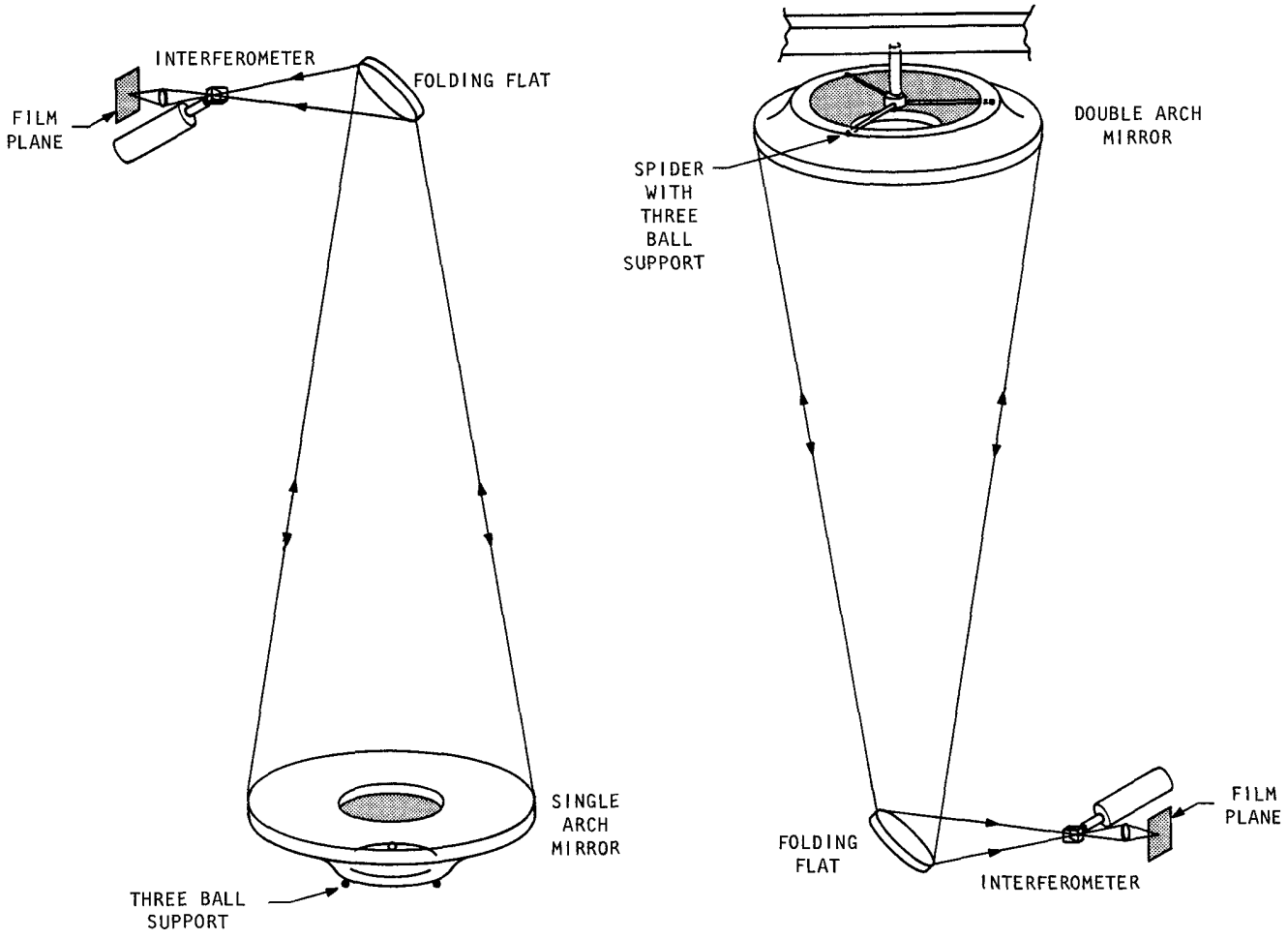

Figure 3. Test arrangements used to determine the gravity deflections.

coefficients. The 36 polynomials are listed in Table 1. The polynomial description was used to generate an optical path difference contour map of the surface of the mirror and to calculate an rms and peak-to-valley residual surface error departure from a perfect sphere. After averaging, the OPD maps for the face-up case were subtracted from the face-down case to detect any changes in shape that occurred independently of the residual figure error on the mirrors.

Table 1. Zernike Polynomials Used by FRINGE in the Order Stored in the Computer

#	Polynomial
1	$r\cos\theta$
2	$r\sin\theta$
3	$2r^2 - 1$
4	$r^2\cos2\theta$
5	$r^2\sin2\theta$
6	$(3r^2-2)r\cos\theta$
7	$(3r^2-2)r\sin\theta$
8	$6r^4 - 6r^2 + 1$
9	$r^3\cos3\theta$
10	$r^3\sin3\theta$
11	$(4r^2-3)r^2\cos2\theta$
12	$(4r^2-3)r^2\sin2\theta$
13	$(10r^4-12r^2+3)r\cos\theta$
14	$(10r^4-12r^2+3)r\sin\theta$
15	$20r^6 - 30r^4 + 12r^2 - 1$
16	$r^4\cos4\theta$
17	$4^4\sin4\theta$
18	$(5r^2-4)r^3\cos3\theta$
19	$(5r^2-4)r^3\sin3\theta$
20	$(15r^4-20r^2+6)r^2\cos2\theta$
21	$(15r^4-20r^2+6)r^2\sin2\theta$
22	$(35r^6-60r^4+30r^2-4)r\cos\theta$
23	$(35r^6-60r^4+30r^2-4)r\sin\theta$
24	$70r^8 - 140r^6 + 90r^4 - 20r^2 + 1$
25	$r^5\cos5\theta$
26	$r^5\sin5\theta$
27	$(6r^2-5)r^4\cos4\theta$
28	$(6r^2-5)r^4\sin4\theta$
29	$(21r^4-30r^2+10)r^3\cos3\theta$
30	$(21r^4-30r^2+10)r^3\sin3\theta$
31	$(56r^6-105r^4+60r^2-10)r^2\cos2\theta$
32	$(56r^6-105r^4+60r^2-10)r^2\sin2\theta$
33	$(126r^8-280r^6+210r^4-60r^2+5)r\cos\theta$
34	$(126r^8-280r^6+210r^4-60r^2+5)r\sin\theta$
35	$252r^{10} - 630r^8 + 560r^6 - 210r^4 + 30r^2 - 1$
36	$924r^{12} - 2772r^{10} + 3150r^8 - 1680r^6 + 420r^4 - 42r^2 + 1$

To better understand and illustrate the resulting deformations, the 36 Zernike polynomials describing the surfaces were divided into groups based on common angular functions. This type of analysis resolves the surface into its angular components of (1) 0θ terms or the purely radial terms, (2) 1θ terms or the comatic terms, (3) 2θ terms or the astigmatic terms, and (4) 3θ terms or the "three-cornered hat" terms. There are in addition to these terms 4θ and 5θ terms that were not included in the study because their contributions were in the noise level. The deformations that did occur were principally changes in the 3θ terms since the support system has threefold angular symmetry.

The results of these analyses are shown in Figures 4 through 7. To help interpret the contour maps note that the residual errors are printed at the bottom of each map along with the 36 Zernike coefficients. The order of the coefficients is read line by line from left to right and corresponds in direct order to the Zernike polynomials listed in Table 1. The contour plots depict the surface error heights scaled in units of waves at 6328 Å. The interior circle drawn on each contour map shows the radial location of the support hub and the three-ball support locations are indicated by the three black spots on the circle. The circle is drawn to scale and the ball locations are indicated correctly in azimuth.

Figure 4 shows the surface figure for the single arch mirror (Mirror #1) resting on the three-ball support, and Figure 5 depicts the surface figure in the hanging support. Moving along the maps in sequence, the total error at the top is broken down into the 1θ terms, the 2θ terms, the 3θ terms, and finally the 0θ or pure radial terms. Notice that the largest error is astigmatism or 2θ error. Figures 6 and 7 depict the deformations of the double arch mirror (Mirror #2) accompanied by the same functional breakdown as shown in Figures 4 and 5. In Figures 4 through 7 the figure errors shown are a combination of the residual polishing errors plus an error due to mounting i.e., the error due to the deformation of the mirror under self-weight as it rests on the three-point support.

To find just the mount-induced errors, the total error under the two different mounting conditions must be subtracted. In Figures 8 and 9 these differences are shown as the error in the face-up condition subtracted from the error in the face-down or hanging condition for the single arch and double arch, respectively. These differences, then, represent twice the 1-g deflection of the mirrors in the mounting. As in the previous figures the total deflection is at the top followed by a breakdown of the difference into its angular components. The results of this analysis are summarized in Table 2.

These results indicate that the single arch is about twice as stiff as the double arch in this type of mounting. This seems to be principally due to the single arch's azimuthal stiffness evidenced by the much larger 3θ deflection of the double arch. It appears that the greater bending moment in the larger support ring of the double arch is the cause since the deflection is coincident with the position of the supports.

(a)

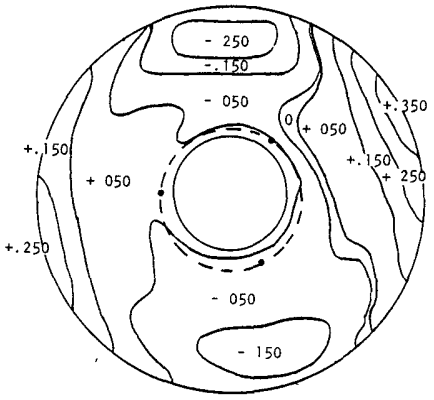

	PTS	RMS	MAX	MIN	SPAN	STREHL
RESIDUALS	672	114	380	- 300	680	601

ZERNIKE POLYNOMIAL COEFFICIENTS

000	000	000	.220	089	.012	-.029	.111	.000
.074	026	.018	- 008	021	-.031	- 049	015	-.002
.008	- 022	- 011	- 007	013	071	- 010	- 034	004
-.006	- 006	-.016	002	- 004	006	- 011	-.073	.026

(b)

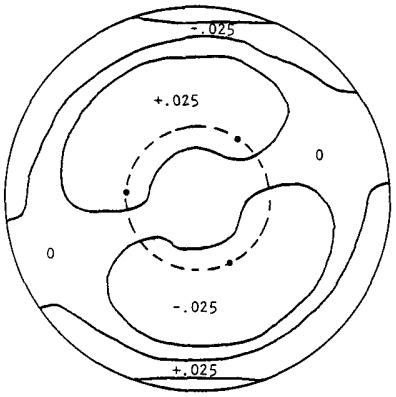

	PTS	RMS	MAX	MIN	SPAN	STREHL
RESIDUALS	672	011	030	- 030	.061	995

ZERNIKE POLYNOMIAL COEFFICIENTS

000	000	.000	000	000	012	-.029	000	.000
.000	.000	000	000	000	000	000	.000	.000
000	000	000	000	000	.000	000	000	000
.000	000	000	000	000	000	000	000	.000

(c)

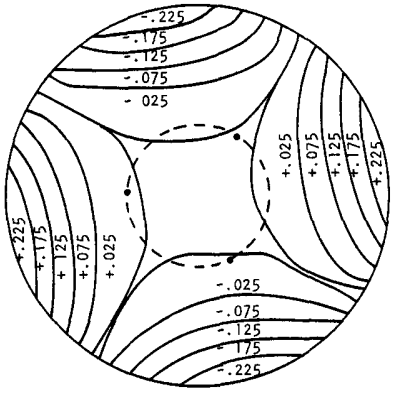

	PTS	RMS	MAX	MIN	SPAN	STREHL
RESIDUALS	672	099	232	- 232	464	679

ZERNIKE POLYNOMIAL COEFFICIENTS

000	000	000	220	089	.000	000	000	.000
.000	.026	.018	000	000	000	000	000	000
000	- 022	- 011	000	000	.000	000	000	000
000	000	.000	002	-.004	.000	.000	000	000

(d)

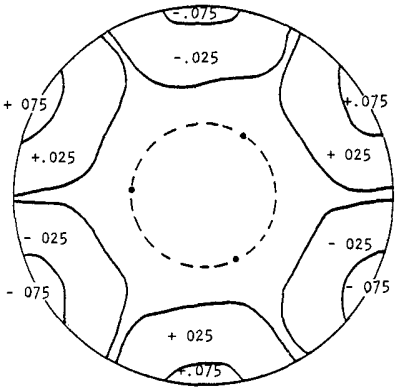

	PTS	RMS	MAX	MIN	SPAN	STREHL
RESIDUALS	672	027	.067	- 067	135	971

ZERNIKE POLYNOMIAL COEFFICIENTS

.000	000	000	000	000	000	000	000	000
.074	.000	000	000	.000	000	.000	.000	- 002
.008	000	000	000	000	.000	000	000	.000
.000	- 006	- 016	000	000	.000	.000	.000	000

(e)

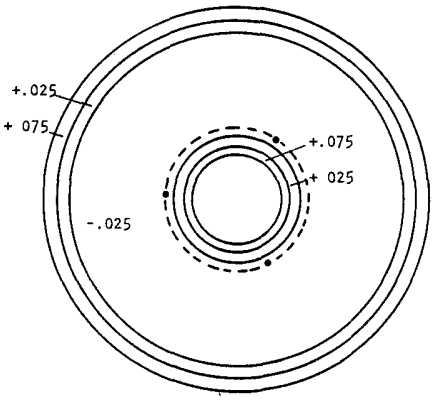

	PTS	RMS	MAX	MIN	SPAN	STREHL
RESIDUALS	672	040	113	- 038	151	.938

ZERNIKE POLYNOMIAL COEFFICIENTS

.000	000	000	000	000	000	000	111	.000
000	000	000	.000	000	-.031	000	000	000
.000	.000	000	000	000	070	000	.000	000
000	.000	.000	000	.000	000	000	-.073	026

Figure 4. Surface figure for the single arch mirror resting on its back on a three-ball support. Plot (a) shows the total figure error described by the 36 Zernike coefficients listed at the bottom. This is followed by an angular breakdown into (b) the 1θ terms, (c) the 2θ terms, (d) the 3θ terms, (e) the 0θ or purely radial terms.

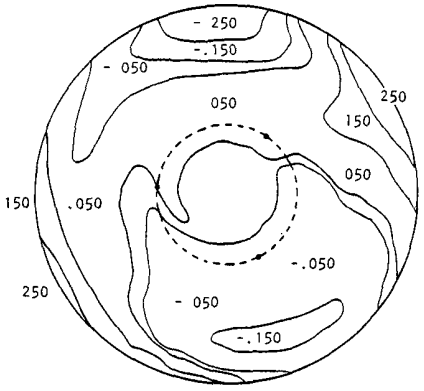

(a)

	PTS	RMS	MAX	MIN	SPAN	STREHL
RESIDUALS	672	097	321	- 284	605	688

ZERNIKE POLYNOMIAL COEFFICIENTS

000	000	000	126	116	019	- 102	.059	- 002
080	.036	025	- 030	030	022	- 058	023	- 004
006	- 050	001	016	013	034	- 008	- 026	019
- 016	- 008	-.011	010	- 002	- 005	-.013	- 049	005

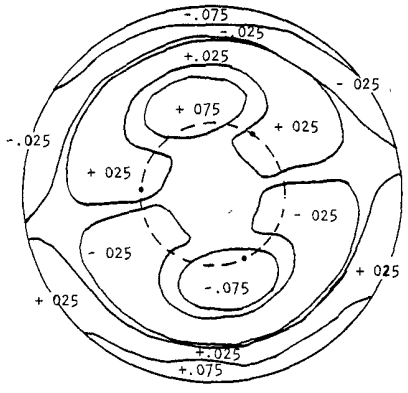

(b)

	PTS	RMS	MAX	MIN	SPAN	STREHL
RESIDUALS	672	038	102	- 102	204	946

ZERNIKE POLYNOMIAL COEFFICIENTS

000	.000	000	000	000	019	-.102	000	.000
000	.000	000	000	000	000	000	.000	.000
.000	.000	000	000	000	.000	.000	.000	.000
000	.000	000	000	000	.000	000	000	000

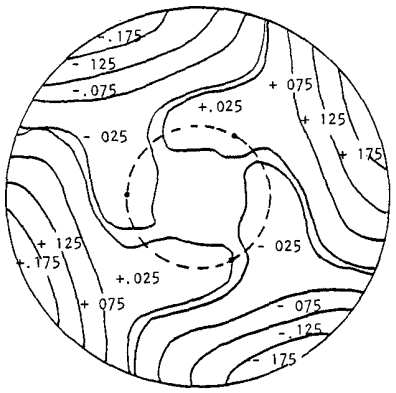

(c)

	PTS	RMS	MAX	MIN	SPAN	STREHL
RESIDUALS	672	075	181	- 181	363	801

ZERNIKE POLYNOMIAL COEFFICIENTS

000	.000	.000	126	116	000	000	000	.000
000	036	025	000	.000	000	000	.000	000
000	-.050	001	000	000	.000	000	000	000
.000	.000	.000	010	- 002	000	000	.000	000

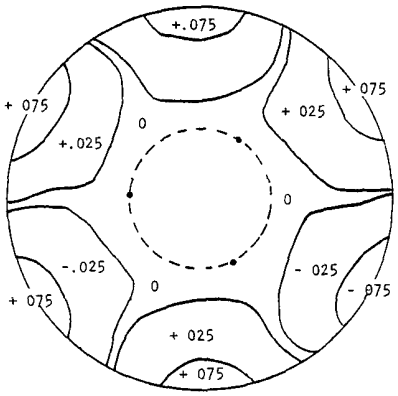

(d)

	PTS	RMS	MAX	MIN	SPAN	STREHL
RESIDUALS	672	029	075	- 075	150	966

ZERNIKE POLYNOMIAL COEFFICIENTS

000	000	000	000	000	000	000	000	- 002
080	000	000	000	000	000	000	000	- 004
006	000	000	000	000	.000	000	000	000
000	-.008	- 011	000	000	000	000	000	000

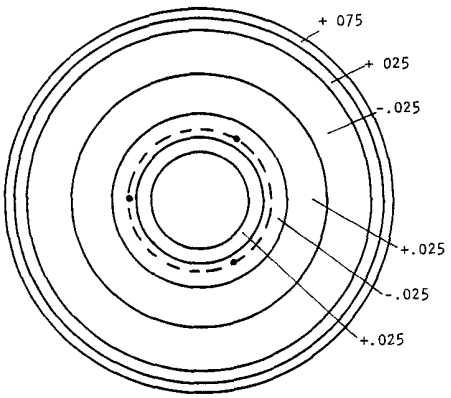

(e)

	PTS	RMS	MAX	MIN	SPAN	STREHL
RESIDUALS	672	029	075	- 040	115	967

ZERNIKE POLYNOMIAL COEFFICIENTS

.000	000	.000	000	000	000	000	059	000
.000	000	000	000	000	022	000	000	000
.000	.000	.000	000	000	.034	000	000	.000
000	000	000	.000	000	000	000	- 049	.005

Figure 5. Surface figure for the single arch mirror in the hanging mode. Plot (a) shows the total figure error described by the 36 Zernike coefficients listed at the bottom. This is followed by an angular breakdown into (b) the 1θ terms, (c) the 2θ terms, (d) the 3θ terms, (e) the 0θ or purely radial terms.

(a)

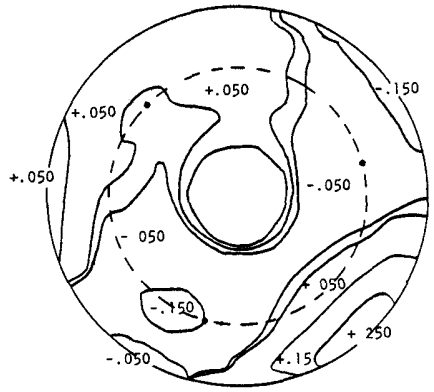

	PTS	RMS	MAX	MIN	SPAN	STREHL
RESIDUALS	672	.081	.276	- 218	.494	.774

ZERNIKE POLYNOMIAL COEFFICIENTS

.000	.000	.000	-.017	- 141	-.009	-.058	.057	-.083
-.057	009	-.021	- 014	.002	-.087	.010	.014	.020
009	.005	.001	-.003	.007	.030	- 008	.010	.002
006	-.009	.006	007	- 010	007	.001	- 047	032

(b)

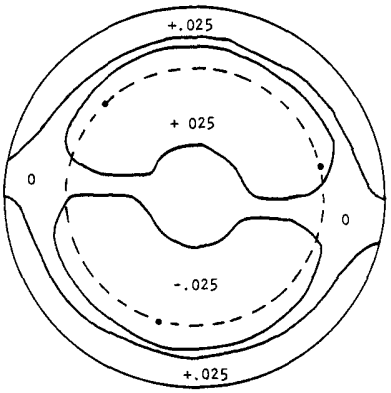

	PTS	RMS	MAX	MIN	SPAN	STREHL
RESIDUALS	672	021	058	- 058	116	.982

ZERNIKE POLYNOMIAL COEFFICIENTS

.000	.000	.000	000	000	- 009	- 058	000	000
.000	.000	.000	000	000	000	.000	.000	000
.000	.000	.000	.000	000	.000	000	.000	.000
000	.000	.000	.000	000	000	.000	000	.000

(c)

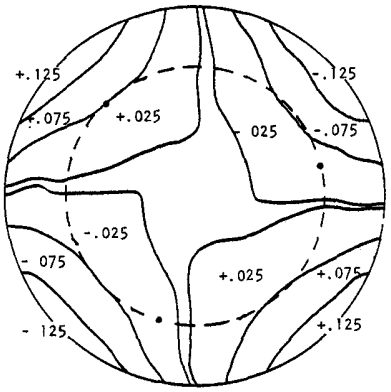

	PTS	RMS	MAX	MIN	SPAN	STREHL
RESIDUALS	672	062	165	- 165	.331	858

ZERNIKE POLYNOMIAL COEFFICIENTS

000	.000	.000	-.017	-.141	000	000	.000	.000
.000	.009	- 021	.000	.000	.000	000	.000	.000
.000	005	.001	.000	.000	000	.000	.000	000
.000	.000	.000	007	- 010	.000	.000	.000	000

(d)

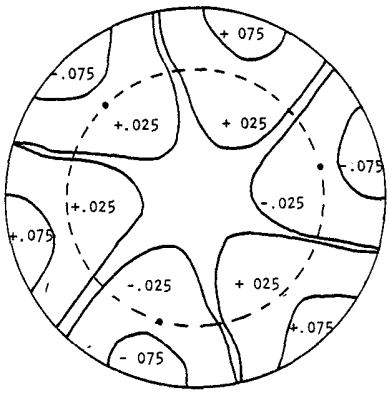

	PTS	RMS	MAX	MIN	SPAN	STREHL
RESIDUALS	672	037	.082	-.082	.164	.946

ZERNIKE POLYNOMIAL COEFFICIENTS

.000	.000	.000	.000	000	000	.000	.000	-.083
-.057	.000	.000	000	.000	.000	000	000	.020
.009	000	.000	000	000	000	.000	.000	.000
.000	- 009	.006	000	.000	000	.000	.000	000

(e)

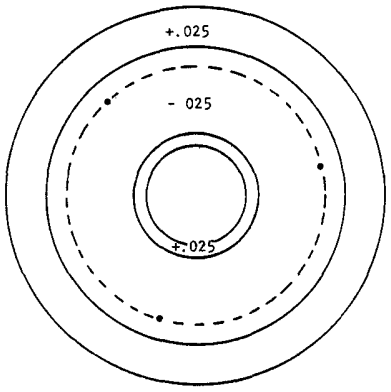

	PTS	RMS	MAX	MIN	SPAN	STREHL
RESIDUALS	672	027	069	-.034	.104	.972

ZERNIKE POLYNOMIAL COEFFICIENTS

.000	.000	.000	.000	.000	000	.000	.057	000
.000	.000	000	.000	.000	-.087	000	.000	.000
.000	.000	.000	000	000	.030	000	000	.000
.000	.000	.000	.000	.000	.000	000	- 047	.032

Figure 6. Surface error of the double arch mirror resting on the three-ball support. Plot (a) shows the total figure error described by the 36 Zernike coefficients listed at the bottom. This is followed by an angular breakdown into (b) the 1θ terms, (c) the 2θ terms, (d) the 3θ terms, (e) the 0θ or purely radial terms.

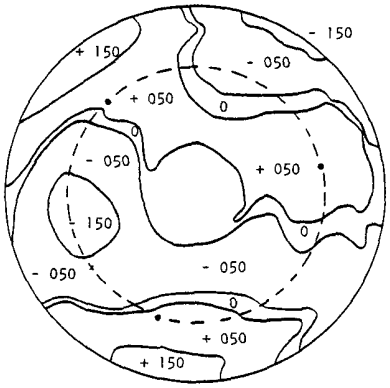

(a)

	PTS	RMS	MAX	MIN	SPAN	STREHL
RESIDUALS	672	065	182	- 199	381	512

ZERNIKE POLYNOMIAL COEFFICIENTS

.000	000	000	- 043	- 046	-.077	-.044	046	082
070	022	-.014	- 015	027	- 076	000	011	- 022
- 015	009	- 006	020	- 012	.022	- 007	- 003	005
- 010	019	.010	004	- 008	-.003	011	- 050	030

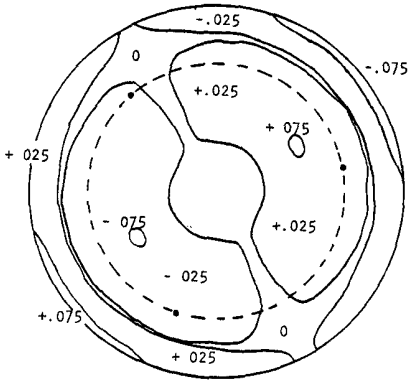

(b)

	PTS	RMS	MAX	MIN	SPAN	STREHL
RESIDUALS	672	032	.088	- 088	176	.960

ZERNIKE POLYNOMIAL COEFFICIENTS

.000	000	000	000	000	- 077	- 044	.000	000
000	000	.000	000	000	.000	.000	.000	.000
000	.000	000	.000	000	000	000	.000	.000
000	000	.000	000	.000	000	.000	.000	000

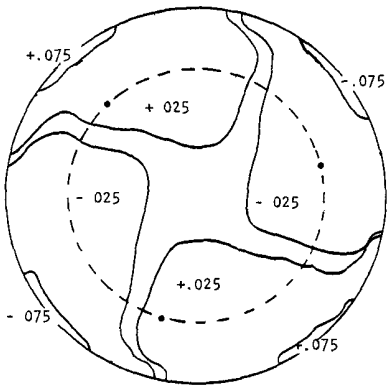

(c)

	PTS	RMS	MAX	MIN	SPAN	STREHL
RESIDUALS	672	029	073	- 073	147	968

ZERNIKE POLYNOMIAL COEFFICIENTS

000	.000	.000	- 043	- 046	.000	000	000	000
000	022	-.014	000	000	.000	000	.000	.000
000	009	- 006	000	.000	000	000	000	000
000	000	.000	004	- 008	000	000	000	.000

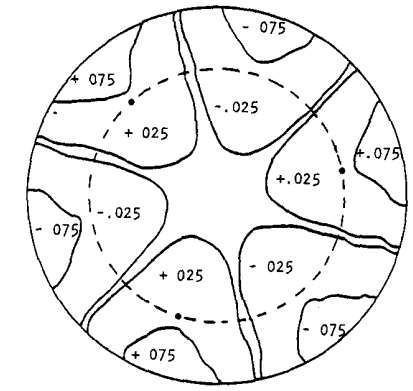

(d)

	PTS	RMS	MAX	MIN	SPAN	STREHL
RESIDUALS	672	041	098	- 098	195	937

ZERNIKE POLYNOMIAL COEFFICIENTS

000	000	000	000	000	.000	000	000	.082
070	000	.000	.000	.000	000	000	000	- 022
- 015	000	000	000	000	000	000	.000	.000
000	019	.010	.000	000	000	000	000	000

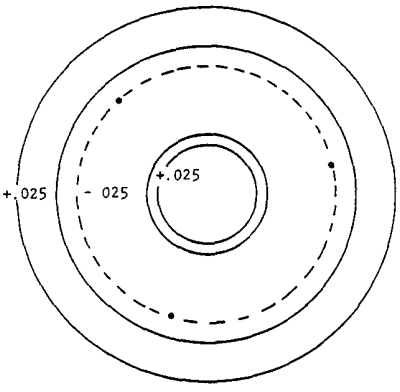

(e)

	PTS	RMS	MAX	MIN	SPAN	STREHL
RESIDUALS	672	024	056	- 030	086	978

ZERNIKE POLYNOMIAL COEFFICIENTS

.000	.000	.000	000	000	000	000	046	000
000	000	000	000	000	-.076	000	000	000
000	000	000	.000	000	022	.000	000	000
.000	000	000	000	.000	.000	000	- 050	030

Figure 7. Surface error of the double arch mirror hanging from the three-ball support. Plot (a) shows the total figure error described by the 36 Zernike coefficients listed at the bottom. This is followed by an angular breakdown into (b) the 1θ terms, (c) the 2θ terms, (d) the 3θ terms, (e) the 0θ or purely radial terms.

(a)

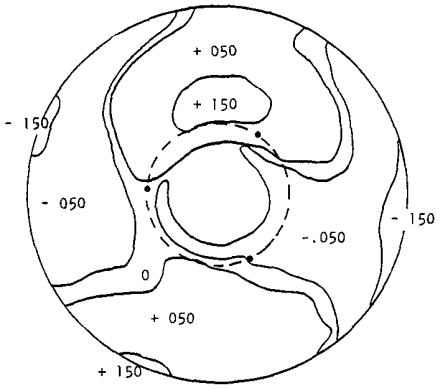

	PTS	RMS	MAX	MIN	SPAN	STREHL
RESIDUALS	672	054	138	- 148	286	870

ZERNIKE POLYNOMIAL COEFFICIENTS

.000	.000	000	-.094	027	007	-.073	- 052	- 002
006	010	.007	- 022	009	053	- 009	008	- 002
- 002	- 028	.012	023	000	- 037	002	.008	015
- 010	- 002	005	.008	002	- 011	- 002	.024	- 021

(b)

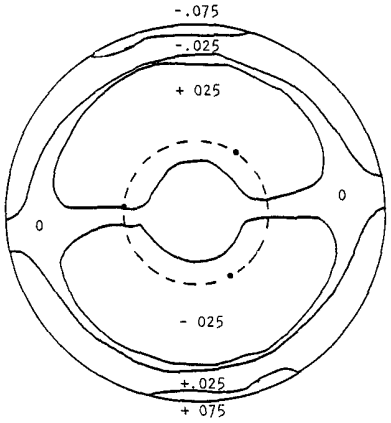

	PTS	RMS	MAX	MIN	SPAN	STREHL
RESIDUALS	672	027	073	-.073	146	973

ZERNIKE POLYNOMIAL COEFFICIENTS

000	000	000	000	000	007	- 073	000	000
000	000	000	.000	000	.000	.000	000	000
000	000	000	000	000	000	000	000	000
000	000	000	.000	000	.000	000	000	000

(c)

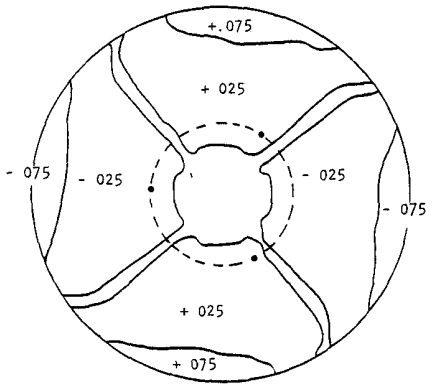

	PTS	RMS	MAX	MIN	SPAN	STREHL
RESIDUALS	672	042	106	- 106	211	934

ZERNIKE POLYNOMIAL COEFFICIENTS

000	000	000	- 094	027	000	000	000	000
000	.010	007	000	000	000	000	000	000
000	- 028	.012	000	000	000	000	000	000
000	000	000	008	002	000	000	000	000

(d)

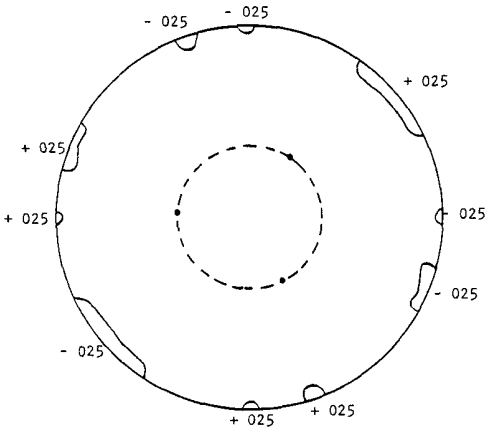

	PTS	RMS	MAX	MIN	SPAN	STREHL
RESIDUALS	672	003	010	- 010	019	1 000

ZERNIKE POLYNOMIAL COEFFICIENTS

000	000	000	000	000	000	000	000	- 002
005	000	000	000	000	000	000	000	- 002
- 002	000	000	000	000	000	000	000	000
000	- 002	005	000	000	000	000	000	000

(e)

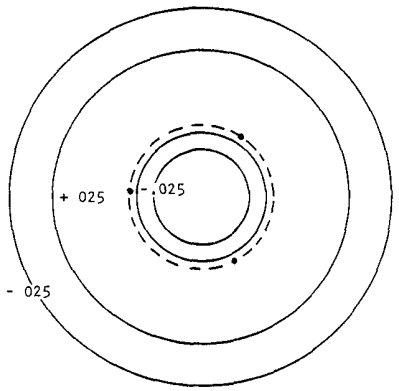

	PTS	RMS	MAX	MIN	SPAN	STREHL
RESIDUALS	672	020	026	- 057	083	985

ZERNIKE POLYNOMIAL COEFFICIENTS

000	000	000	000	000	000	000	- 052	000
000	000	000	000	000	.053	000	000	000
000	000	000	000	000	- 036	000	000	000
000	000	.000	000	000	000	000	024	- 021

Figure 8. The 2-g deflections of the single arch mirror and its angular functional breakdown. Plot (a) shows the total figure error described by the 36 Zernike coefficients listed at the bottom. This is followed by an angular breakdown into (b) the 1θ terms, (c) the 2θ terms, (d) the 3θ terms, (e) the 0θ or purely radial terms.

(a)

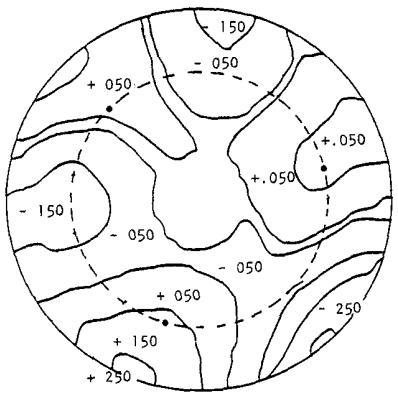

	PTS	RMS	MAX	MIN	SPAN	STREHL
RESIDUALS	672	094	243	- 356	.599	.707

ZERNIKE POLYNOMIAL COEFFICIENTS

.000	000	.000	-.027	095	- 068	014	-.011	164
.126	013	.007	- 001	025	011	- 010	-.004	- 042
- 024	004	- 007	023	-.018	-.008	001	- 013	003
- 016	028	.003	- 003	002	- 010	010	- 002	- 003

(b)

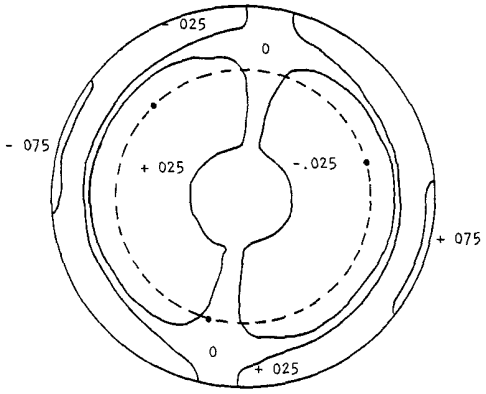

	PTS	RMS	MAX	MIN	SPAN	STREHL
RESIDUALS	672	.025	068	- 068	136	975

ZERNIKE POLYNOMIAL COEFFICIENTS

000	000	000	000	.000	068	- 014	000	000
000	000	000	000	000	000	000	000	000
000	000	000	000	.000	.000	000	000	.000
000	.000	000	.000	000	.000	000	.000	000

(c)

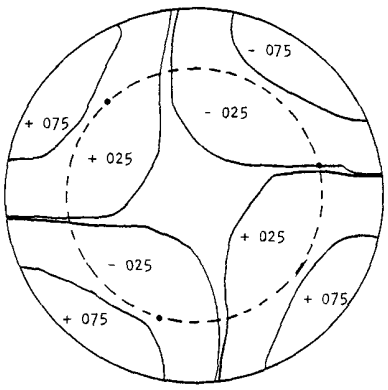

	PTS	RMS	MAX	MIN	SPAN	STREHL
RESIDUALS	672	043	.096	-.096	193	.931

ZERNIKE POLYNOMIAL COEFFICIENTS

000	000	000	026	- 095	000	000	000	000
000	- 013	- 007	000	000	000	000	.000	000
000	- 004	007	000	000	000	000	000	000
000	000	000	003	- 002	000	000	.000	000

(d)

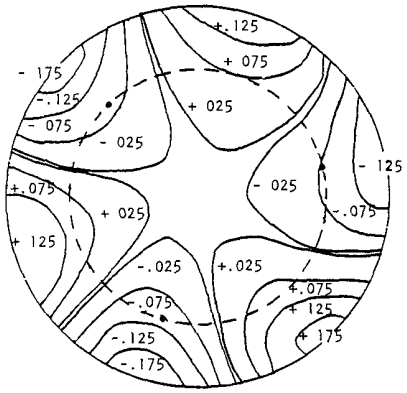

	PTS	RMS	MAX	MIN	SPAN	STREHL
RESIDUALS	672	.078	196	- 199	395	787

ZERNIKE POLYNOMIAL COEFFICIENTS

000	000	.000	000	.000	.000	.000	000	- 165
- 127	.000	000	000	000	000	000	042	024
000	000	.000	000	.000	000	000	.000	.000
- 028	000	000	000	000	000	000	000	000

(e)

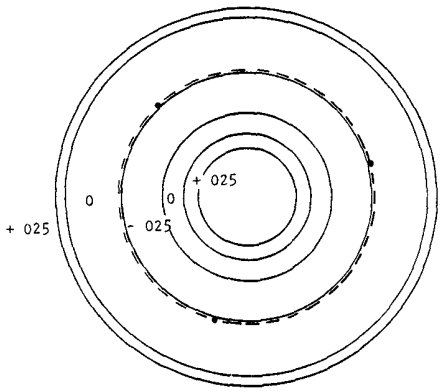

	PTS	RMS	MAX	MIN	SPAN	STREHL
RESIDUALS	672	005	014	-.008	022	999

ZERNIKE POLYNOMIAL COEFFICIENTS

000	000	000	.000	000	000	.000	011	000
000	000	.000	000	000	- 011	000	000	000
000	000	000	000	000	008	.000	000	000
000	.000	000	000	000	000	000	003	002

Figure 9. The 2-g deflections of the double arch mirror and its angular functional breakdown. Plot (a) shows the total figure error described by the 36 Zernike coefficients listed at the bottom. This is followed by an angular breakdown into (b) the 1θ terms, (c) the 2θ terms, (d) the 3θ terms, (e) the 0θ or purely radial terms.

Table 2. Self-weight (2 g) Deflections

	Mirror #1 Single arch		Mirror #2 Double arch	
	P-V (waves at 6328 Å)	Rms (waves at 6328 Å)	P-V (waves at 6328 Å)	Rms (waves at 6328 Å)
Total deflection	0.286	0.054	0.599	0.094
1θ terms	0.146	0.027	0.136	0.025
2θ terms	0.211	0.042	0.193	0.043
3θ terms	0.019	0.003	0.395	0.078
Radial	0.083	0.020	0.022	0.005

However, the radial stiffness of the double arch appears to be about four times that of the single arch as evidenced by the purely radial deflections in both cases. Perhaps with a more uniform support on the double arch's support ring, its azimuthal deflection could be improved and its greater radial stiffness could be utilized. The radial deflection does not include any radius change that may have occurred which may, in fact, be the largest deflection. A focal shift cannot be detected in this type of analysis since the deformations described by the Zernike polynomials are always minimized with respect to a spherical surface centered at the diffraction focus, which may be shifted from one test to another. If the system in which the mirror is used can be refocused, this will present no difficulty. Both mirrors appear to behave about the same with respect to astigmatism and coma.

A finite element analysis was performed on the double arch mirror with three support points, and the expected gravity deflections were calculated. The results of this analysis are shown in Figure 10. This analysis shows a peak-to-valley error of 0.205 λ in a three-cornered hat shape that agrees fairly well with the measured peak-to-valley value of 0.299 λ having the same three-cornered hat shape.

Measurement error analysis

In an effort to assess the effect of various sources of noise on the data reduction process, an experiment was run to find out the repeatability of the interferogram digitization process. In the first part of the experiment, a single interferogram was digitized 10 times without making any changes whatever between the 10 digitizations. It was found that the mean rms figure error was 0.087 ± 0.001 λ and the mean peak-to-valley error was 0.442 ± 0.013 λ.

In the actual course of digitization, each new interferogram is randomly placed in a different location on the data tablet before it is digitized. In the second part of the experiment, the same interferogram as used in the first part was moved to a new location each time. The results this time were slightly more noisy as might be expected. The mean rms error was 0.438 ± 0.019 λ.

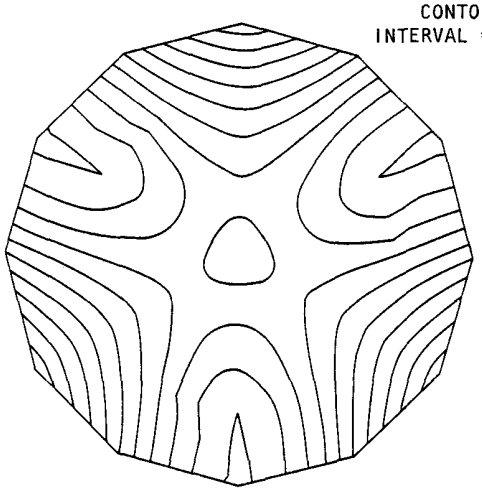

Figure 10. Finite element analysis of the double arch's 1-g deflections. Compare this with half the values of Figure 9.

Since the averages in the actual mirror tests were based on four different interferograms, we would have expected standard deviations larger than those in the experiment by $\sqrt{10}/\sqrt{4} = 1.58$ were the noise due only to digitization and data reduction. During the mirror testing there were six averages of four interferograms. These averages yielded a standard deviation of 0.107 λ on the peak-to-valley averages. Thus it is seen (Table 3) that the variation from interferogram to interferogram due to air turbulence and vibration in the test setup is far larger than the noise contributed by the digitization process. Recall too that when two quantities are differenced, the standard deviation of the difference is the root sum square of the standard deviations of the quantities being differenced. This was the process used to establish the standard deviations on the difference contour maps representing the changes due to mounting conditions and heat treating.

Conclusions

Supported horizontally on three points, the single arch mirror has about half the total deflection of the double arch design. The calculation of the total deflection does not provide an estimate of any change in the radius of curvature that may have occurred under

Table 3. Standard Deviations

	P-V (λ)	rms (λ)
Same interferogram reduced four times (not moved)	0.021	0.002
Same interferogram reduced four times (moved each time)	0.030	0.005
Four different interferograms of the same test condition	0.107	0.016
Estimated σ's for difference maps containing all 36 terms	0.151	0.023

gravity loads in the test, but modal and zonal deflections from the sphere are clearly revealed by the FRINGE analysis performed. The single arch mirror is twice as stiff azimuthally as the double arch, but radially the double arch has 4 times the stiffness of the single arch. If a more uniform azimuthal support were provided for the double arch, its deflections would be expected to improve significantly.

From the repeatability tests and the observations about standard deviations during these tests, differences larger than 0.02 λ rms and 0.15 λ peak-to-valley represent real changes in mirror figure in the 36-term fit. Similarly bounds may be calculated for individual Zernike terms should these be of interest. In particular, we would not expect the uncertainty in the radial terms to be as great as those with angular dependence due to their circular symmetry.

The errors involved in the determination of the deflections are not limited by the reduction process but by the testing conditions. The errors could be reduced by reducing vibration and more importantly air turbulence. Also, since the variance is a decreasing function of order number, the mirrors should not contain large low order figure errors when attempting to detect small changes.

The ease of fabrication of the single arch and the double arch mirrors is roughly the same, the only distinction being the steeper inner contour of the double arch that required some more care and time.

Acknowledgment

This work was sponsored by NASA under contract NAS2-10903.

References

1. Jacobs, S. F., and D. Shough, "Thermal Expansion Uniformity of Hereaus-Amersil TO8E Fused Silica," Appl. Opt., Vol. 20, pp. 3461-3464, 1981.
2. S. F. Jacobs, to be published.
3. Vukobratovich, D., et al., "Optimum Shapes for Lightweighted Mirrors," Proc. SPIE, Vol. 332, 1982.
4. Miller, G. H., et al., Proc. SPIE, Vol. 332, 1982.
5. Loomis, John S., FRINGE User Manual Version 2, Optical Sciences Center, University of Arizona, Tucson, Arizona, November 1976.